JOURNAL OF COMPUTATIONAL PHYSICS **127,** 412–423 (1996)
ARTICLE NO. 0184

Zonal Embedded Grids for Numerical Simulations of Wall-Bounded Turbulent Flows

A. G. KRAVCHENKO,* P. MOIN,* AND R. MOSER†

*Department of Mechanical Engineering, Stanford University, Stanford, California 94305; †Department of Theoretical and Applied Mechanics, University of Illinois at Urbana-Champaign, Urbana, Illinois 61801

Received November 3, 1995; revised April 16, 1996

A B-spline based numerical method on a zonal embedded grid has been developed. The method is aimed at reducing the computational requirements for large eddy simulations (LES) and direct numerical simulations (DNS) of wall-bounded turbulent flows. The objective is to reduce the number of grid points required to resolve the near-wall eddies without placing a large number of grid points in the outer layers. DNS and LES calculations of a turbulent channel flow were performed on a grid with a zone near the wall that was refined in all three directions. The results from the zonal grid calculations show good agreement with previously published numerical and experimental results obtained for the same flow conditions. The zonal grid calculations required only a fraction of the CPU time required for the single zone grid calculation with the same near-wall grid density. In addition, the memory requirements for the zonal grid calculations are significantly reduced.

1. INTRODUCTION

Direct numerical and large eddy simulations (DNS and LES) have been widely used to study the physics of turbulence. However, turbulence simulations have been limited to flows in simple geometries. The computations of flows in complex geometries are still very expensive.

In wall-bounded turbulent flows, the near-wall flow structures are small compared to the overall flow dimensions. These small structures play an important role in the dynamics of turbulent boundary layers and should be well resolved. In typical computations of mean flow, grid-stretching in the direction normal to the wall is used to resolve large mean velocity gradients. However, in turbulence simulations a fine mesh is also required near the wall in the directions parallel to the wall. This fine resolution is normally extended into the outer layers where it is not required.

The grid refinement in near-wall regions can be done more efficiently with zonal embedded grids. In this approach, several regions (zones) of grids are constructed in such a way that the mesh spacing decreases from zone to zone as one approaches the wall. One can also choose to combine grid-stretching in one direction with zonal embedding in the other two. This technique permits a fine grid to be embedded near the wall without placing a large number of grid points in the outer layers. As a result, the total number of grid points is reduced which leads to savings in CPU time and memory.

A pacing item for large eddy simulations of high Reynolds number flows of engineering interest is an accurate treatment of the near-wall turbulence structures. As pointed out by Moin and Jimenéz [1], the near wall structures are the important large eddies, so they cannot be treated accurately with subgrid scale parameterizations. Instead, they need to be resolved or completely modeled with dynamic wall functions [2–3]. An efficient computation of these structures can be achieved with zonal grids. This is an important step in computation of higher Reynolds number flows of aerodynamic interest.

Zonal grid techniques have been mostly used with finite-difference or finite-volume methods to resolve solution and/or geometry complexity in computations of compressible [4–6] and incompressible [7–8] flows. In these studies, a particular concern has been the numerical treatment of the regions where zones with different grid densities meet. Usually, a high-order accurate interpolation procedure is required to exchange information between zones. Also, a special treatment of the internal grid boundaries is necessary to maintain conservation. However, in many cases, it is difficult to achieve both high accuracy and conservation at the same time with finite difference or finite volume methods on zonal grids [6].

The objective of our study is to develop an efficient method for turbulence simulations on zonal embedded grids and test its accuracy and consistency. In particular, we want to study the effect of zonal boundaries on turbulent eddies crossing them. In this paper, we consider problems where turbulence is inhomogeneous in one direction (y) and homogeneous in the other two directions (x and z). However, the approach can be extended to the case of two or three inhomogeneous directions. In the homogeneous directions, we use Fourier spectral methods [9]. A Galerkin method with B-spline basis functions [10] is used

0021-9991/96 $18.00

in the inhomogeneous direction. B-splines as basis-functions have been used in several numerical studies [11–13] to solve a variety of time-dependent test problems. For simulations on zonal embedded grids, a B-spline based method appears to offer many advantages over other numerical methods. B-splines have local support which leads to banded matrices that can be efficiently stored and solved. They also provide high accuracy and are C^{k-1} continuous (where k is the order of a B-spline) which allows velocity derivatives to be accurately and smoothly represented. The construction of the higher order B-splines is done using a recursive relationship which makes implementation of a B-spline based method straightforward. B-splines can be defined on any type of grid distribution and, thus, provide great flexibility in choosing a grid-stretching based on the physics of a problem. A method based on B-splines does not experience the difficulties of finite-difference methods in maintaining conservation properties and handling physical and zonal boundary conditions.

The numerical method is tested on simple model problems which include the evolution of small disturbances in channel flow and a vortex dipole rebound from a wall. These tests indicated that B-spline methods have the potential of accurately simulating unsteady flows. The latter test also showed that the eddies can pass through the embedded zones without noticeable distortions. The method also proved to be both accurate and cost-effective. Furthermore, DNS and LES calculations of fully developed turbulent channel flow were carried out in order to compare simulations on zonal embedded grids with existing numerical and experimental results.

The numerical method is briefly outlined in Section 2. The implementation of a zonal grid structure is presented in Section 3. Numerical tests are described in Section 4, followed by a summary in Section 5.

2. GOVERNING EQUATIONS AND THE NUMERICAL METHOD

We consider incompressible flows governed by the Navier–Stokes equations,

$$\frac{\partial \mathbf{u}}{\partial t} = H - \nabla P + \frac{1}{\mathrm{Re}} \nabla^2 \mathbf{u}, \tag{1}$$

$$\nabla \cdot \mathbf{u} = 0, \tag{2}$$

where Re is the Reynolds number, $\mathbf{u} = (u, v, w)$ is the velocity vector, and $H = \mathbf{u} \times \boldsymbol{\omega} = (H_u, H_v, H_w)$ is the convective term. Following the same approach as in [14] one can reduce Eqs. (1) and (2) to a fourth-order equation for v and a second-order equation for the normal component of vorticity g,

$$\frac{\partial}{\partial t} \nabla^2 v = h_v + \frac{1}{\mathrm{Re}} \nabla^4 v, \tag{3}$$

$$\frac{\partial}{\partial t} g = h_g + \frac{1}{\mathrm{Re}} \nabla^2 g, \tag{4}$$

$$f + \frac{\partial v}{\partial y} = 0, \tag{5}$$

where

$$f = \frac{\partial u}{\partial x} + \frac{\partial w}{\partial z}, \quad g = \frac{\partial u}{\partial z} - \frac{\partial w}{\partial x}, \tag{6}$$

$$h_v = -\frac{\partial}{\partial y}\left(\frac{\partial H_u}{\partial x} + \frac{\partial H_w}{\partial z}\right) + \left(\frac{\partial^2}{\partial x^2} + \frac{\partial^2}{\partial z^2}\right) H_v, \tag{7}$$

$$h_g = \frac{\partial H_u}{\partial z} - \frac{\partial H_w}{\partial x}. \tag{8}$$

Let $\tilde{\mathbf{u}}$ be a numerical approximation to $\mathbf{u}$. Using the method of weighted residuals, we obtain the discrete weak forms of Eqs. (3) and (4),

$$\int_V \xi \frac{\partial}{\partial t} \nabla^2 \tilde{v}\, dV = \int_V \xi \tilde{h}_v\, dV + \int_V \xi \frac{1}{\mathrm{Re}} \nabla^4 \tilde{v}\, dV, \tag{9}$$

$$\int_V \zeta \frac{\partial}{\partial t} \tilde{g}\, dV = \int_V \zeta \tilde{h}_g\, dV + \int_V \zeta \frac{1}{\mathrm{Re}} \nabla^2 \tilde{g}\, dV, \tag{10}$$

where ξ and ζ are the weight functions, which we select to be

$$\begin{aligned} \xi(x, y, z) &= e^{-ik'_x x} e^{-ik'_z z} B_i^k(y), \\ \zeta(x, y, z) &= e^{-ik'_x x} e^{-ik'_z z} B_i^{k-1}(y). \end{aligned} \tag{11}$$

The numerical approximation of the velocity vector $\tilde{\mathbf{u}} = (\tilde{u}, \tilde{v}, \tilde{w})$ is written in terms of spectral and B-spline functions,

$$\tilde{v}(x, y, z, t) = \sum_{k_x, j, k_z} \hat{v}_j(k_x, k_z, t) e^{ik_x x} e^{ik_z z} B_j^k(y), \tag{12}$$

$$\begin{pmatrix} \tilde{u} \\ \tilde{w} \end{pmatrix}(x, y, z, t) = \sum_{k_x, j, k_z} \begin{pmatrix} \hat{u}_j(k_x, k_z, t) \\ \hat{w}_j(k_x, k_z, t) \end{pmatrix} e^{ik_x x} e^{ik_z z} B_j^{k-1}(y), \tag{13}$$

where $B_j^k(y)$ is the B-spline of order k [10]. B-spline functions of order k are defined on a set of knot points t_j by the recursive relationship

$$B_j^k(y) = \frac{(y - t_j)}{(t_{j+k} - t_j)} B_j^{k-1}(y) + \frac{(t_{j+k+1} - y)}{(t_{j+k+1} - t_{j+1})} B_{j+1}^{k-1}(y), \tag{14}$$

where a B-spline of order zero is a top hat function; i.e., $B_j^0(y) = 1$ if $t_j \le y \le t_{j+1}$ and 0 otherwise. An example of

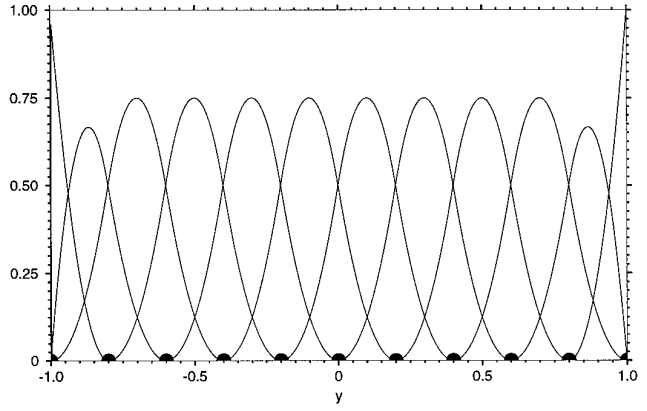

FIG. 1. Second-order B-splines shown on a uniform 10-point knot set. Knot points are indicated with ●.

the quadratic B-splines ($k = 2$) defined on a uniformly spaced set of 10 knots is shown in Fig. 1. Note that all interior B-splines are zero at the boundaries. Only the boundary B-splines are nonzero at the boundary points. This property will be exploited later to impose boundary conditions.

The v-velocity is represented in terms of B-splines which are one order higher than the B-spline expansion functions for u and w. This allows the continuity equation, Eq. (5), to be satisfied exactly by the numerical representation.

Evaluating the integrals in Eqs. (9) and (10), we obtain matrix equations for $\hat{\mathbf{v}}$ and $\hat{\mathbf{g}}$ for each independent Fourier mode (k_x, k_z),

$$\mathbf{M}_v \frac{d\hat{\mathbf{v}}}{dt} = \mathbf{D}_v \hat{\mathbf{v}} + \mathbf{R}_v(\hat{\mathbf{u}}, \hat{\mathbf{v}}, \hat{\mathbf{w}}), \tag{15}$$

$$\mathbf{M}_g \frac{d\hat{\mathbf{g}}}{dt} = \mathbf{D}_g \hat{\mathbf{g}} + \mathbf{R}_g(\hat{\mathbf{u}}, \hat{\mathbf{v}}, \hat{\mathbf{w}}), \tag{16}$$

where $\mathbf{R}_v$, $\mathbf{R}_g$ are the expressions resulting from the nonlinear terms and $\mathbf{M}_v$, $\mathbf{M}_g$, $\mathbf{D}_v$, $\mathbf{D}_g$ are banded matrices with elements given by

$$m_{ij}^v = -(k_x^2 + k_z^2) \int B_i^k B_j^k \, dy + \int B_i^k \frac{\partial^2}{\partial y^2} B_j^k \, dy,$$

$$m_{ij}^g = \int B_i^{k-1} B_j^{k-1} \, dy,$$

$$d_{ij}^v = \frac{1}{\mathrm{Re}} \left[(k_x^2 + k_z^2)^2 \int B_i^k B_j^k \, dy - 2(k_x^2 + k_z^2) \int B_i^k \frac{\partial^2}{\partial y^2} B_j^k \, dy + \int B_i^k \frac{\partial^4}{\partial y^4} B_j^k \, dy \right],$$

$$d_{ij}^g = \frac{1}{\mathrm{Re}} \left[-(k_x^2 + k_z^2) \int B_i^{k-1} B_j^{k-1} \, dy + \int B_i^{k-1} \frac{\partial^2}{\partial y^2} B_j^{k-1} \, dy \right].$$

The number of diagonals in the matrices is just $2k + 1$, where k is the order of the B-splines. Also note, that for N_y knot points there are $N_y + k$ B-splines of order k and $N_y + k - 1$ B-splines of order $k - 1$. Accordingly, there are $N_y + k$ B-spline coefficients for v and $N_y + k - 1$ B-spline coefficients for u, w, and g.

The boundary conditions are imposed strongly. Consider the boundary conditions for a channel flow that follow from the no-slip conditions at the walls ($y = \pm 1$),

$$\tilde{v}(x, \pm 1, z, t) = \frac{\partial}{\partial y} \tilde{v}(x, \pm 1, z, t) = \tilde{g}(x, \pm 1, z, t) = 0.$$

Setting the B-spline coefficients,

$$\hat{v}_1 = \hat{v}_2 = \hat{v}_{N_y+k-1} = \hat{v}_{N_y+k} = \hat{g}_1 = \hat{g}_{N_y+k-1} = 0, \tag{17}$$

will satisfy these boundary conditions. For brevity in (17), we used $\hat{v}_j = \hat{v}_j(k_x, k_z, t)$. Note that since the boundary conditions (17) are imposed strongly, the use of integration by parts to modify the matrix elements in Eqs. (15) and (16) does not introduce boundary terms. For example, the last term in the expression for d_{ij}^v can be written as

$$\int B_i^k \frac{\partial^4}{\partial y^4} B_j^k \, dy = \int \frac{\partial^2}{\partial y^2} B_i^k \frac{\partial^2}{\partial y^2} B_j^k \, dy.$$

The time-advancement is carried out with a semi-implicit scheme that uses Crank–Nicholson for the viscous terms and third-order Runge–Kutta for the nonlinear terms [15]. All time-dependent simulations were performed with variable time steps and at a CFL number never exceeding $\sqrt{3}$, as required by the stability of the third-order Runge–Kutta scheme.

To compute the nonlinear terms $\mathbf{R}_v$ and $\mathbf{R}_g$, the integrals involving h_v and h_g in Eqs. (9) and (10) must be evaluated. As an example, consider one term in the expression for h_v and the resulting integral,

$$\int_V e^{-ik_x' x} e^{-ik_z' z} B_l^k(y) \frac{\partial}{\partial y} \tilde{v} \frac{\partial \tilde{u}}{\partial y} \, dx \, dy \, dz.$$

All the other terms are similar. In the x and z directions, the integral is evaluated using numerical quadrature on a uniform mesh. By using $\frac{3}{2}$ as many quadrature points in each direction as Fourier modes, the quadratures are made exact. This is dealiasing by the $\frac{3}{2}$ rule. The quadratures in y are evaluated using precomputed integrals of the products of B-splines and their derivatives. The computations are accomplished by evaluating the B-spline coefficients of the velocity components $(\tilde{u}, \tilde{v}, \tilde{w})$ as functions of x and z on the quadrature points using fast Fourier transforms (FFTs). The y integrals can then be evaluated as

$$\sum_m \sum_n \left[\int B_l^k(y) \frac{\partial}{\partial y} \left(B_m^k(y) \frac{\partial}{\partial y} B_n^{k-1}(y) \right) dy \right] \tilde{v}_m \tilde{u}_n = \sum_m \sum_n I_{lmn} \tilde{v}_m \tilde{u}_n \tag{18}$$

at each quadrature point, where the integral in brackets (I_{lmn}) can be precomputed exactly. Since the B-splines have local support, I_{lmn} is nonzero only if $|l - m| \leq k$, $|l - n| \leq k$ and $|m - n| \leq k$. Thus, the sums in (18) can be evaluated in order $N_b k^2$ operations, where N_b is the number of B-splines used in the y direction. Once (18) and the other terms have been evaluated, the quadrature sums in the x and z directions are evaluated using FFTs.

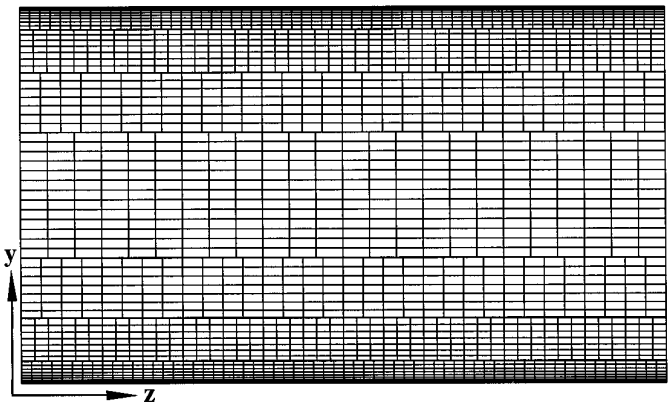

FIG. 2. Zonal embedded grid with fine grid zones near the walls and coarse zones in the middle.

3. ZONAL GRID IMPLEMENTATION

The motivation for zonal embedded grids is to use them in large eddy simulations of complex turbulent flows. This section presents the grid resolution requirements in the near-wall and outer layers for large eddy simulations of wall-bounded turbulent flows and describes the implementation of a zonal embedded grid.

The average streamwise and spanwise scales of near-wall flow structures are of the order $500\nu/u_\tau$ and $100\nu/u_\tau$, respectively, [14], where u_τ is the shear velocity and ν is the kinematic viscosity. Experience with LES of channel flows indicates that adequate resolution of these structures requires minimum grid spacings in the near-wall region: $\Delta x^+ \simeq 120$ and $\Delta z^+ \simeq 25$, where + indicates a nondimensionalization by shear velocity u_τ and kinematic viscosity ν. For simulations of turbulent channel flow at $\mathrm{Re}_\tau = u_\tau \delta/\nu = 4000$ on the domain $L_x = 2\pi\delta$, $L_y = 2\delta$, and $L_z = \pi\delta/2$ this translates into $N_x \simeq 192$ in the streamwise direction and $N_z \simeq 256$ in the spanwise direction. In the outer layer, turbulent eddy sizes scale with δ (where δ is the boundary layer thickness), and the average resolution is about $\Delta x = \Delta z \simeq \delta/10$ [16], which requires $N_x \simeq 64$ and $N_z \simeq 16$ points. Such grid requirements can be most efficiently satisfied with zonal grids. However, a smooth mesh size transition from the near-wall region to the outer layer is desirable to avoid problems associated with truncation errors. This is achieved with several intermediate zones.

A cross section of a typical 3D zonal embedded "grid" for a channel flow simulation is shown in Fig. 2. The horizontal grid lines are the knots of the spline representation of the vertical direction and the vertical lines represent the Nyquist spatial sampling rate required for the Fourier representation of the solution at each y location. Note that both the vertical and horizontal grid resolution varies with y, with the horizontal resolution changing in steps. The y-locations of these step changes are called zonal boundaries. The variation of the horizontal resolution in y is accomplished by simply varying the ranges of the k_x and k_z sums in the representations (12) and (13) with the B-spline index j. The k_x and k_z ranges of the weight functions (11) are varied similarly. Since the B-splines are local in y, this has the desired effect. However, each interior B-spline has support on $k + 1$ knot intervals, so there is overlap between B-splines associated with different horizontal resolutions. Thus, the actual change in horizontal resolution takes place over k knot intervals, which is expected to soften the effect of the resolution change.

The important issue that arises in all zonal embedded grid studies is the influence of the zonal boundaries on the eddies that cross them. We address this question in studies of a vortex dipole rebounding from a wall and the numerical simulation of a turbulent channel flow (see below).

4. RESULTS AND DISCUSSION

This section presents some results of the numerical tests that have been conducted to assess the performance of the B-spline method and zonal embedded grids. It also contains the results of direct numerical and large eddy simulations of fully developed turbulent channel flows at Reynolds numbers up to $\mathrm{Re}_c = U_c\delta/\nu \sim 1.1 \times 10^5$.

4.1. *Solution of the Orr–Sommerfeld Stability Equation*

In this test, we consider the most unstable linear instability mode of a plane Poiseuille flow with the wavenumber $\alpha = 1$ and $\mathrm{Re} = 10{,}000$ and compare the performance of the B-spline method with that of the Chebyshev method [17]. B-splines are used as expansion functions to approximate solutions of the Orr–Sommerfeld equation:

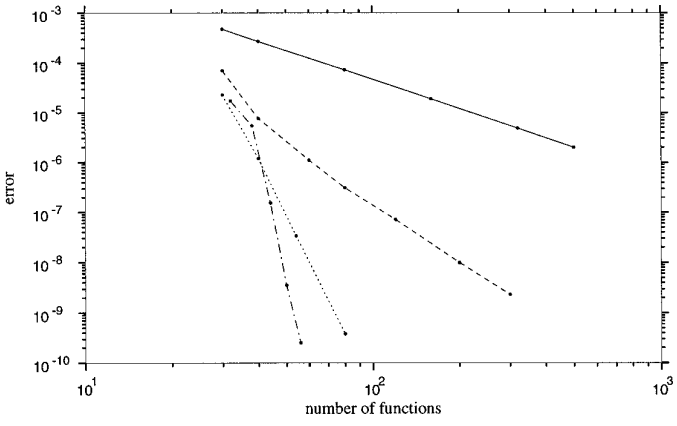

FIG. 3. Errors in eigenvalues obtained with: ———, B-splines of second order; – – –, B-splines of third order; ···, B-splines of fourth order; –·–, Chebyshev polynomials.

$$\left(\frac{d^2}{dy^2}-\alpha^2\right)^2 v - i\alpha\,\mathrm{Re}\,U_o(y)\left(\frac{d^2}{dy^2}-\alpha^2\right)v + i\alpha\,\mathrm{Re}\,U_o''(y)v = -i\omega\alpha\,\mathrm{Re}\left(\frac{d^2}{dy^2}-\alpha^2\right)v, \tag{19}$$

where Re is the Reynolds number, ω is the temporal frequency, and $U_o(y) = 1 - y^2$ is the laminar velocity profile of a Poiseuille flow between parallel planes.

Using the method of weighted residuals with B-splines as expansion and test functions, we obtain a matrix form of Eq. (19):

$$\mathbf{A}\hat{\mathbf{v}} = \omega\mathbf{B}\hat{\mathbf{v}}, \tag{20}$$

where $\hat{v}_i$ are the coefficients in the expansion of v in terms of B-splines. The matrix eigenvalue problem (20) is solved to find the eigenvalue with the largest imaginary part.

Figure 3 shows the relative error of the numerical schemes based on B-splines of various orders. The errors are estimated as $\varepsilon = |\omega_i - \omega_i^0|$, where ω_i^0 is the imaginary part of the most accurately found eigenvalue: $\omega^0 = 0.23752649 + 0.00373967i$. As expected, the higher the order of the B-splines the faster the convergence of the method. The method based on fourth-order B-splines for v-velocity produces results which are very close in accuracy to the results obtained with the spectral Chebyshev method. In fact, by increasing the order of the B-splines we are able to match the performance of the Chebyshev method. However, as was mentioned above, the advantage of the B-splines is that, unlike the Chebyshev polynomials, they provide the flexibility of choosing any type of grid stretching and are spatially compact.

4.2. *Propagation of Small Disturbances in a Channel*

To examine the accuracy and robustness of the numerical method, we study the evolution of small amplitude disturbances in channel flow. When the amplitude of the disturbances imposed on the laminar parabolic profile is small, the solution of Eqs. (1) and (2) is known from the linear theory. The flow field is initialized as

$$u(x, y, t) = 1 - y^2 + \varepsilon u',$$
$$v(x, y, t) = \varepsilon v',$$

where the disturbances u' and v' are taken to be eigensolutions of the Orr–Sommerfeld equation and $\varepsilon = 10^{-4}$ is a small factor.

The numerical value of perturbation energy defined as

$$E(t) = \int_0^{Lx}\int_{-\delta}^{\delta}(u'^2 + v'^2)\,dx\,dy$$

is computed and compared to the exact solution. The particular problem chosen for this test is the same as that described in [18] with one unstable mode for $\mathrm{Re}_c = 7500$, where Re_c is the Reynolds number based on centerline velocity and channel half-width, $\mathrm{Re}_c = U_c\delta/\nu$. In this case, the perturbation energy grows exponentially in time, $E(t)/E(0) = e^{2\omega_i t}$, where $\omega_i = 0.00223498$.

Figures 4 and 5 show the evolution of perturbation energy in the channel for three different grids. B-splines of different order are considered. The results obtained with quadratic and cubic B-splines for v-velocity are shown in Figs. 4 and 5, respectively. The B-splines for u-velocity are always one order lower. In both cases, the results are very inaccurate for small number of mesh points $N_y = 16$. Obviously, the resolution is inadequate in these cases. However, the results for $N_y = 32$ are substantially better. In fact,

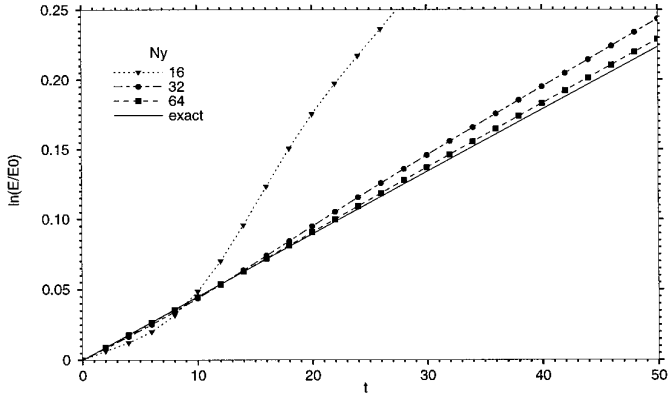

FIG. 4. Perturbation energy growth for channel flow ($\mathrm{Re}_c = 7500$). Fourier spectral method in x and B-spline method in y are used. B-splines of order 2 are used for v-velocity and of order 1 for u-velocity.

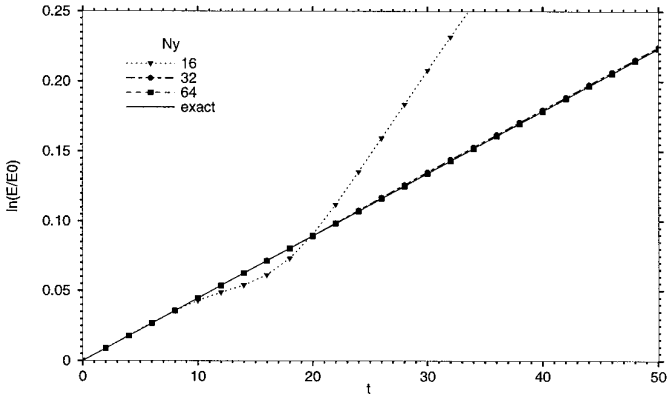

FIG. 5. Perturbation energy growth for channel flow ($\mathrm{Re}_c = 7500$). Fourier spectral method in x and B-spline method in y are used. B-splines of order 3 are used for v-velocity and of order 2 for u-velocity.

cubic B-splines on this mesh produce an energy evolution curve which is virtually identical to the exact curve.

4.3. *Vortex Dipole Rebound from a Wall*

To gain insight into how sudden changes in the grid size affect the dynamics of eddies in turbulent flows, we performed numerical simulations of a two-dimensional vortex dipole impinging on a flat wall [19]. In this test problem, a vortex dipole is introduced in the middle of the channel. As the dipole approaches the lower wall, it creates a region of strong vorticity at the wall. Later in time, this vorticity sheet detaches from the wall to form a secondary vortex pair. The strength of the vorticity decreases continuously due to viscous dissipation.

The Reynolds number of the initial vortex is chosen to be $\mathrm{Re} = \Gamma/\nu = 1800$, where Γ is the circulation of the vortex, and ν is the kinematic viscosity. The size of the computational domain was chosen to be $\pi\delta$ and 2δ in the spanwise and normal directions, respectively, where δ is the channel half-width. The computations were carried out on three different grids which are shown in Fig. 6. A single zone fine grid had 64×64 mesh points. Zonal grids had the near-wall zone with the same resolution as the single zone fine grid and a coarser zone in the middle of the channel. In case 1, the ratio of the fine grid spacing to the coarse grid spacing was $\Delta z_f/\Delta z_c = 0.5$; in case 2, this ratio was $\Delta z_f/\Delta z_c = 0.75$.

Figure 6 shows the vorticity field in the channel at five consecutive times, obtained in simulations on the three grids. It is clear that there is no distortion in the shape and the strength of the vortex dipole due to the presence of the zonal boundary. The differences between the two-zone and single-zone results with the same grid density near the wall are minimal. There are some noticeable differences between the single grid and the case 1 zonal grid calculations at the lowest contour level. These differences are small and they can be reduced by choosing a smaller grid change (as in case 2) or by adding an extra zone to provide a smoother grid transition (not shown).

The strength and the size of these vortices are larger than those of typical eddies in high Reynolds number turbulent flows, but the fact that the zonal boundary does not have a destructive effect on the results is very promising.

4.4. *DNS of Turbulent Channel Flow*

To demonstrate the applicability of the method to computations of turbulent flows, we performed direct numerical simulations of a fully developed turbulent channel flow at Reynolds number $\mathrm{Re}_c = U_c\delta/\nu = 3300$. The simulations were carried out on two grids: a one-zone coarse grid ($64 \times 96 \times 64$) and a three-zone grid with two zones ($96 \times 32 \times 96$) near both walls refined in the streamwise and spanwise directions and one coarse grid zone ($64 \times 32 \times 32$) in the middle of the channel. In both cases, the grid was stretched in the wall-normal direction with a hyperbolic tangent stretching function. Also note that in the case of the zonal grid, the number of grid points in the spanwise direction in the middle zone is smaller than that of the 1-zone coarse grid. As shown later, this grid still provides an adequate resolution and at the same time reduces the CPU time and memory requirements.

The flow field is initialized as

$$\begin{aligned} u(x, y, z, t) &= 1 - y^2 + \varepsilon u', \\ v(x, y, z, t) &= \varepsilon v', \\ w(x, y, z, t) &= \varepsilon w', \end{aligned} \tag{21}$$

where u', v', and w' are random numbers scaled to vary between -1 and 1 and $\varepsilon = 0.1$. Equations (3) and (4) are then integrated in time until the flow field reaches a statistically steady state. Typical computations required six nondimensional time units (tu_τ/δ) to reach statistically steady state and about eight additional time units to accumulate statistics. The simulations were performed at a constant mass flow rate.

The mean velocity profile non-dimensionalized by the wall shear velocity is shown in Fig. 7. The present results are compared to the fine grid DNS of [14] which was done with a spectral method using $128 \times 129 \times 128$ modes. The dashed line shows the results of computations on a 1-zone coarse grid. The velocity profile in this case is below the fine-grid DNS of [14] and the log-law, indicating that there is an inadequate grid resolution in the near-wall region. By switching to a zonal grid with an increased number of grid points in the streamwise and spanwise directions near the walls, we obtain results that are in a very good agreement with the DNS of [14]. In addition, we can further decrease the spanwise grid spacing in the middle zone

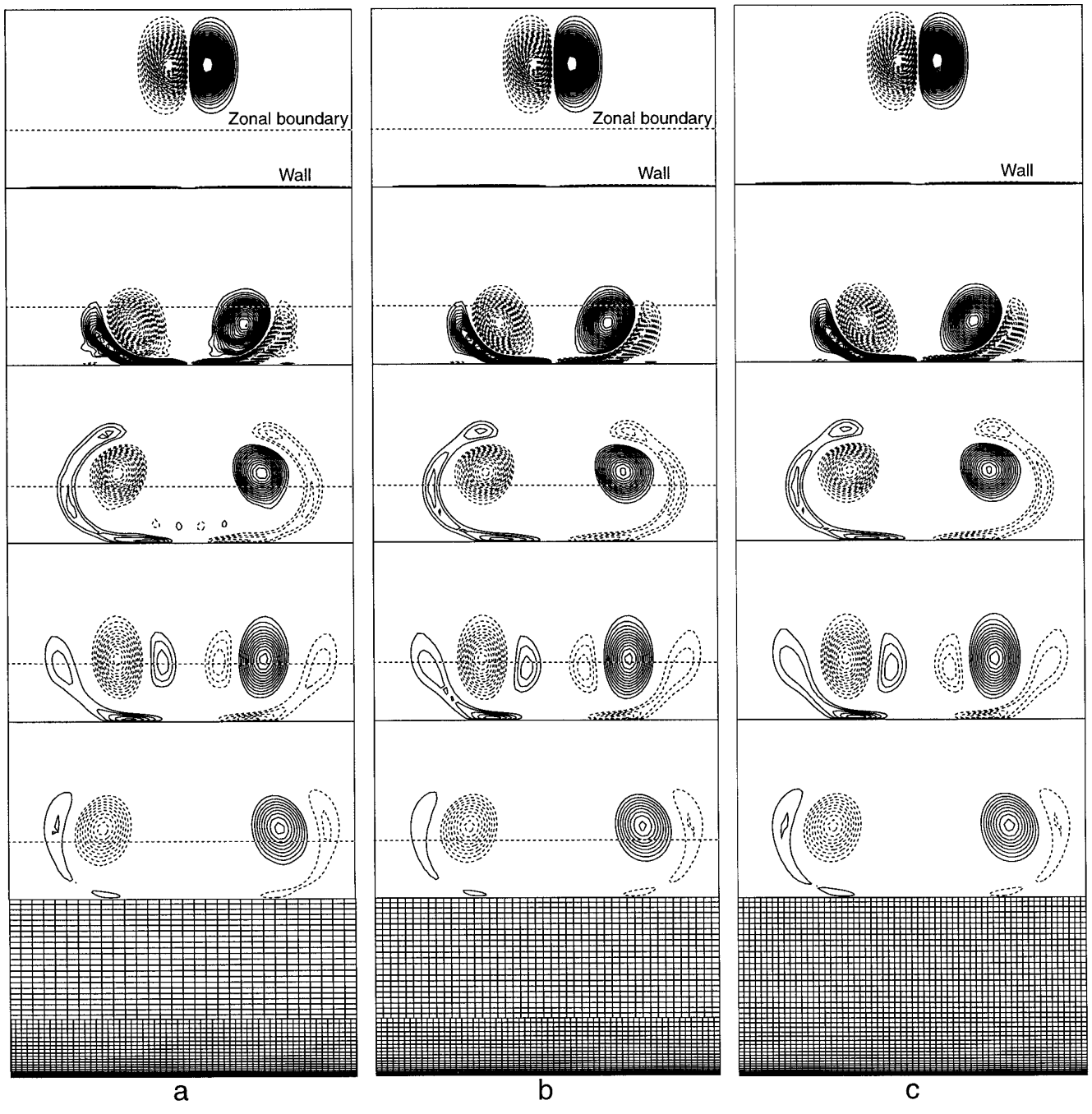

FIG. 6. Time sequence of the evolution of a vortex dipole from $t\Gamma/\delta^2 = 2$ to 26 with increments of 6. Contour levels of the vorticity $\omega_x\delta^2/\Gamma$ range from -10 to 10 by increments of 0.33; negative contours are dashed. (a) Zonal grid with coarse to fine grid size ratio 2; (b) zonal grid with coarse to fine grid size ratio $\frac{4}{3}$; (c) single-zone grid.

without damaging the results but gaining substantial savings in CPU time and memory requirements.

Figure 8 shows the turbulence intensities normalized by the wall shear velocity obtained by zonal grid simulations. The agreement with the fine grid DNS of [14] is very good. Very importantly, there is a smooth transition between the fine grid zone and the coarse grid zone indicating that there is no noticeable impact of the zonal boundaries on the turbulent intensities.

The Reynolds shear stress normalized by the wall shear velocity is shown in Fig. 9. The straight line profile of the total shear stress indicates that the flow has reached an

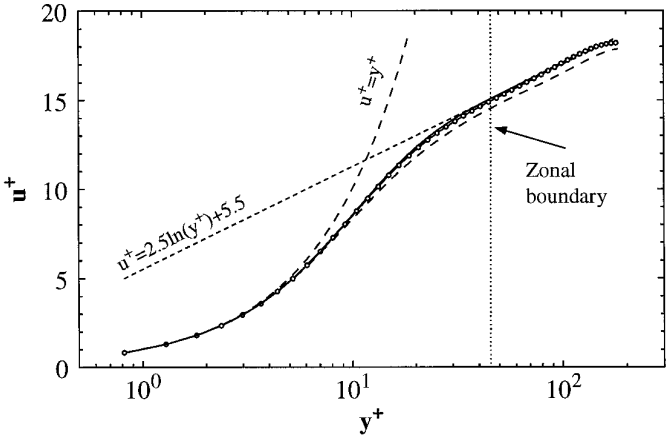

FIG. 7. Mean velocity profile of fully developed turbulent channel flow at $Re_c = 3300$. DNS on 3-zone grid: —○—; DNS of [14]: ———; DNS on 1-zone grid: – – –.

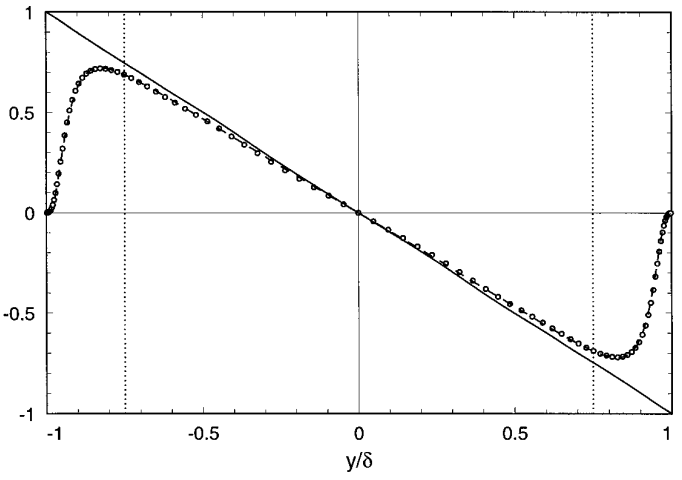

FIG. 9. Reynolds shear stress normalized by the wall shear velocity shown on two grids. Zonal grid DNS: ○, $-\overline{u'v'}$; ———, total shear stress $-\overline{u'v'} + (1/\mathrm{Re})\partial\overline{u}/\partial y$. DNS of [14]: – – –, $-\overline{u'v'}$. Lines ⋯ show the locations of the zonal boundaries.

equilibrium state. The results of the zonal grid simulations are shown, together with the Reynolds shear stress obtained in [14]. Once again, the agreement between these two simulations is excellent, and there is no disruption of the profile at the zonal boundaries.

Figures 10 and 11 show one-dimensional streamwise and spanwise energy spectra in the near-wall region and in the middle of the channel. Here, k_x and k_z are the wave numbers in the streamwise and spanwise directions, respectively. These spectra are in excellent agreement with those shown by Kim *et al.* in [14]. There are reasonable decays in the energy densities and there is no energy pileup at the high wave numbers. The grid resolutions in all grid zones are adequate. Although, the spanwise and streamwise grid spacings in the middle zone are relatively coarse, there is no apparent effect on the energy spectra in the near-wall region. The near-wall one-dimensional energy spectra for the single zone coarse simulations are shown with dashed lines in Fig. 10. In this simulation, the grid in the near-wall region is known to be too coarse. As a result, there is insufficient decay of energy at the high wave numbers in both the streamwise and spanwise spectra.

Comparing the computational requirements for the B-spline method and the Chebyshev polynomials based method used in [14] we found that single zone simulations

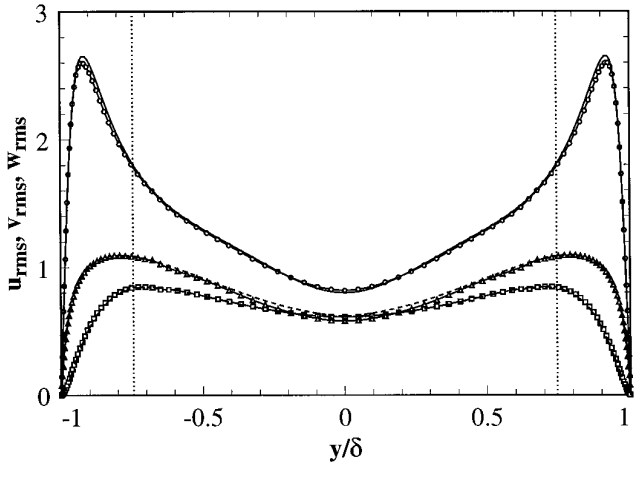

FIG. 8. Root-mean-square velocity fluctuations normalized by the wall shear velocity shown on two grids. Zonal grid DNS: —○—, u_{rms}; —△—, v_{rms}; —□—, w_{rms}. DNS of [14]: ———, u_{rms}; –·–, v_{rms}; – – –, w_{rms}. Lines ⋯ show the locations of the zonal boundaries.

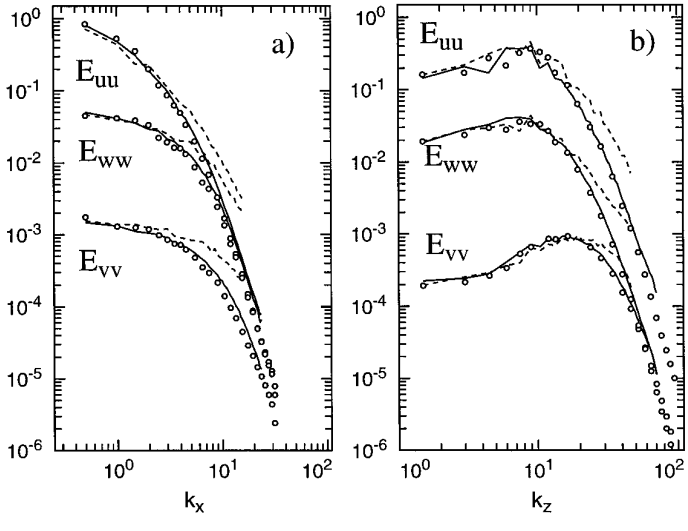

FIG. 10. One-dimensional energy spectra at $y^+ \simeq 5.4$: ———, multi-zone grid; ⋯, single-zone grid; ○, DNS of [14]: (a) streamwise; (b) spanwise.

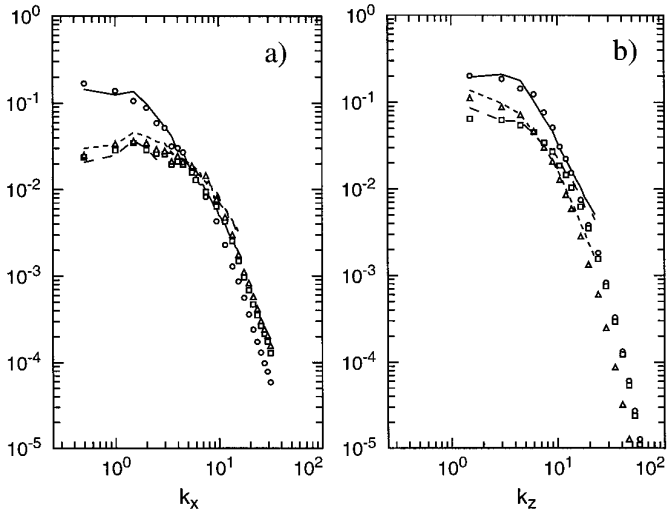

FIG. 11. One-dimensional energy spectra at $y^+ \simeq 128$. Zonal grid DNS: ———, E_{uu}; – – –, E_{vv}; ---, E_{ww}. DNS of [14]: ○, E_{uu}; □, E_{vv}; △, E_{ww}. (a) streamwise; (b) spanwise.

with the B-spline method require about the same amount of CPU time per time step as the method of [14] with the same number of grid points and on the same computer platform (Cray C90). Increasing the order of the B-splines does not cause a significant increase in the overall CPU time per time step. The advantage of the B-spline scheme is the ability to use zonal embedded grids. For example, using zonal grids for simulations of turbulent channel flow at Reynolds number $\mathrm{Re}_c = 3300$ provides an additional 30% reduction in CPU time and memory requirements over single grid simulations of the same flow with the same near-wall resolution. These savings become much more significant in simulations of high Reynolds number flows.

4.5. *LES of Turbulent Channel Flow*

With the present computational capabilities, DNS of turbulent flows at Reynolds numbers of engineering interest are virtually impossible. Alternatively, one can perform large eddy simulations (LES), i.e., compute the dynamically important large scale components of the flows and model the small scales [20–21]. In the present study, we use the dynamic subgrid scale model [20] with the modification of [22]. Grid and test filtering are performed with a Fourier cutoff in the homogeneous directions. In the wall-normal direction, no test filtering is performed. In each homogeneous direction, the ratio of the test filter width to the grid filter width was 2.

We performed large eddy simulations of a fully developed turbulent channel flow at $\mathrm{Re}_m = 2U_m\delta/\nu = 4.631 \times 10^4$ and $\mathrm{Re}_m = 1.915 \times 10^5$, where U_m is the bulk velocity defined by $U_m = (1/2\delta) \int_{-\delta}^{\delta} U(y)\, dy$. A summary of all computed cases is presented in Table I. In the wall normal direction the resolution was $0.6 \leq \Delta y^+ \leq 130$ in cases 1 and 2 and $1.0 \leq \Delta y^+ \leq 100$ in case 3. In the first two cases, the B-splines of order 3 (for v-velocity) and 2 for (u- and w-velocities) were used. The B-splines of order 2 and 1 were used in the last case.

The flow was initialized as in the case of DNS (see Eq. (21)). All simulations were performed with a constant mass flow. In the beginning, the computations were carried out on a single-zone coarse grid until a turbulent mean velocity profile was obtained. Then, the computations were continued on a multi-zone grid to a statistically steady state and compared to the results of the single-zone coarse grid simulations and experiments. Typical computations required four nondimensional time units (tu_τ/δ) to reach a statistically steady state and approximately six additional time units to accumulate statistics. The distribution of grid points for the cases considered is shown in Fig. 12.

Figure 13 shows the mean velocity profile nondimensionalized by the wall shear velocity for cases 1 and 2. The symbols represent the experimental data of [23, 24] obtained at Reynolds numbers $\mathrm{Re}_c = 23{,}191$ and $\mathrm{Re}_c = 22{,}776$, respectively. The dashed lines represent the law of the wall, and the log-law, $u^+ = 2.44 \ln y^+ + 5.0$. The dotted line shows the velocity profile obtained on a single zone coarse grid, $32 \times 64 \times 24$. The mean velocity profile of this simulation falls above the log-law and the experimental data due to the insufficient resolution in the near-wall region. The zonal embedded grid simulation is in a good agreement with the experimental measurements. The results were improved by just refining the near-wall region.

TABLE I

Summary of LES Computations

Case	$\mathrm{Re}_m = \frac{2U_m\delta}{\nu}$	$\mathrm{Re}_c = \frac{U_c\delta}{\nu}$	$\mathrm{Re}_\tau = \frac{u_\tau\delta}{\nu}$	Number of zones	Near-wall grid spacing
1	4.631×10^4	2.606×10^4	1110	1	$\Delta x^+ \simeq 220$, $\Delta z^+ \simeq 70$
2	4.631×10^4	2.624×10^4	1140	5	$\Delta x^+ \simeq 110$, $\Delta z^+ \simeq 20$
3	1.915×10^5	1.094×10^5	3990	9	$\Delta x^+ \simeq 130$, $\Delta z^+ \simeq 20$

Note. U_m, U_c, and u_τ are bulk, centerline, and shear velocities, respectively.

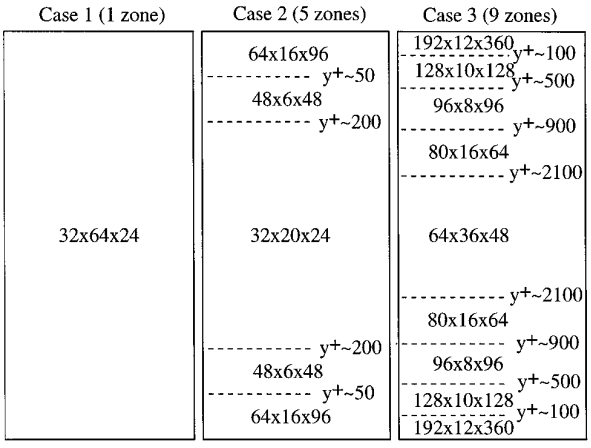

FIG. 12. Grid point distribution and y^+-locations of zonal boundaries in LES of turbulent channel flow.

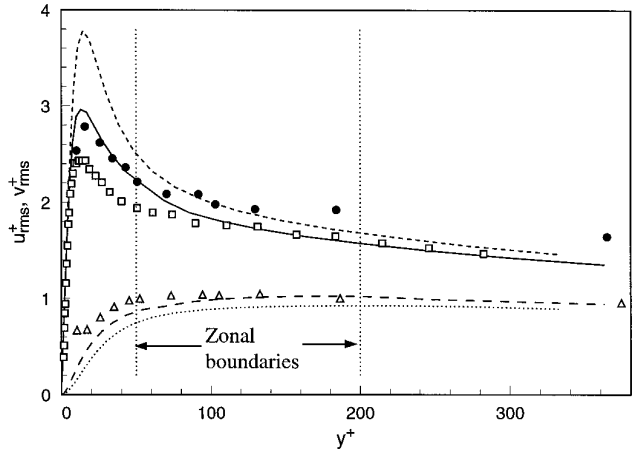

FIG. 14. Root-mean-square velocity fluctuations normalized by the wall shear velocity. LES of fully developed turbulent channel flow at Re_c = 26,241. ———, u_{rms} on multi-zone embedded grid; ---, u_{rms} on single-zone coarse grid; – – –, v_{rms} on multi-zone embedded grid; ···, v_{rms} on single-zone coarse grid; □, Experiment u_{rms} [23], Re_c = 23,191; ●, Experiment u_{rms}, △, Experiment v_{rms} [24], Re_c = 22,776.

The resolvable turbulence intensities normalized by the wall shear velocity are shown in Fig. 14. The maximum of the root-mean-square streamwise velocity fluctuations obtained with one-zone coarse LES is much higher than that obtained in the experiments. This is a typical symptom of a coarse LES computation. The refinement of the grid in the near-wall region alleviates this problem. As the mesh in the near-wall zone is refined in the streamwise and spanwise directions the maximum of the rms of streamwise velocity approaches the experimental data. The overall agreement of the computed turbulence intensities with the experimental results is good.

In addition to the described zonal grid simulations, LES on a single zone grid with approximately the same total number of mesh points as in the zonal grid (64 × 64 × 64) was performed. Although, minor differences between these two simulations were observed in the mean velocity profile, zonal grid simulations exhibited a much better representation of the important turbulent structures in the near-wall region and better turbulence intensities. For example, Fig. 15 and Fig. 16 show spanwise two-point correlations R_{uu} and R_{vv} for the multi-zone and single-zone simulations. The zero crossing and a pronounced negative minimum in the profile of R_{uu} clearly supports the existence of low- and high-speed streaks in the case of zonal grid simulations. These structures are known to be dominant in turbulent boundary layers [25]. The profile of R_{uu} from the single zone computation crosses the z-axis only slightly and shows nonphysical oscillations due to marginal resolution. Thus, in the case of the single grid simulation the

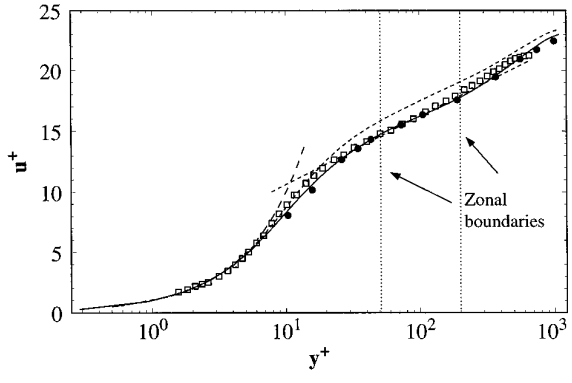

FIG. 13. Mean velocity profile of fully developed turbulent channel flow at Re_c = 26,241. ———, LES on a zonal embedded grid; ---, LES on 1-zone coarse grid; □, Experiment Re_c = 23,191 [23]; ●, Experiment, Re_c = 22,776 [24].

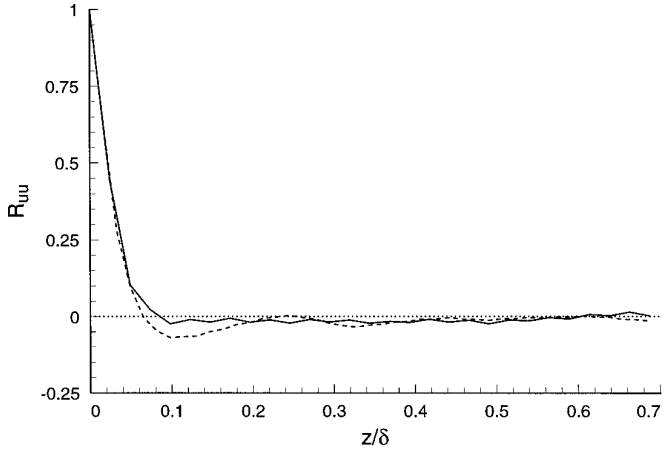

FIG. 15. Spanwise two-point correlations $R_{uu}(z)$ at $y^+ \simeq 20$: ---, multi-zone grid; ———, single zone grid with the same total number of points.

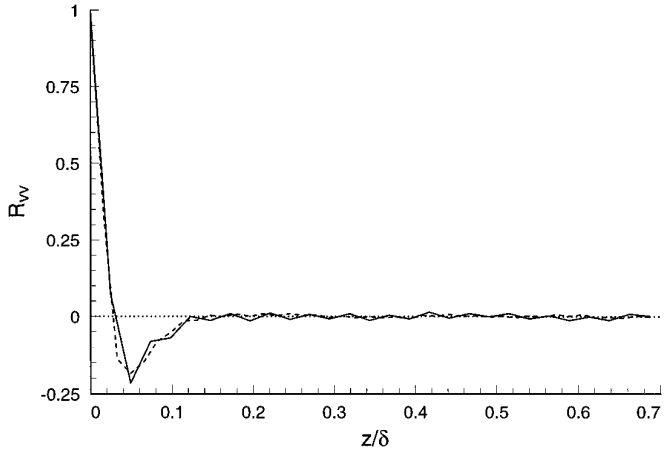

FIG. 16. Spanwise two-point correlations $R_{vv}(z)$ at $y^+ \simeq 20$: ---, multi-zone grid; ———, single zone grid with the same total number of points.

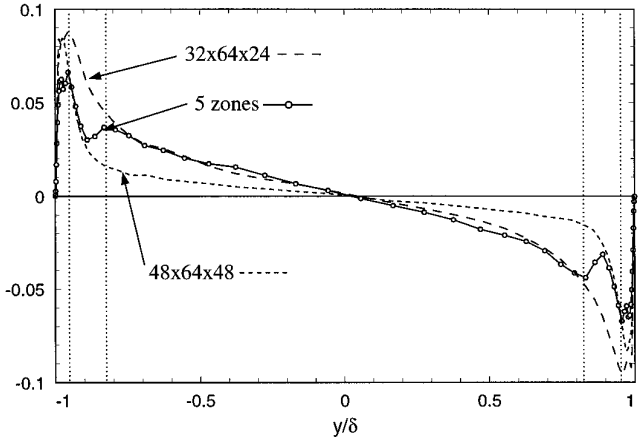

FIG. 18. Subgrid-scale shear stress in LES of turbulent channel flow at $\mathrm{Re}_m = 4.631 \times 10^4$ on various grids: ··· − zonal boundaries.

streaks are not resolved. The minimum of R_{vv} in Fig. 16 indicates the presence of streamwise vortical structures in the wall region. However, in the case of single zone grid, the profile of R_{vv} exhibits nonphysical oscillations. Clearly, the near-wall spanwise resolution is inadequate in this case.

The results of LES at high Reynolds number, Re_c = 109,410, together with the experimental results of Comte-Bellot [26] are shown in Fig. 17. The agreement between the numerical simulations and the experiment is very good. Zonal grids provided an optimal mesh distribution and substantial CPU time savings in the computation of this flow. A single-zone simulation with the same near-wall grid resolution would require almost nine million points and would be much more expensive. A single-zone simulation with the same number of grid points would have an insufficient near-wall resolution and would be inaccurate.

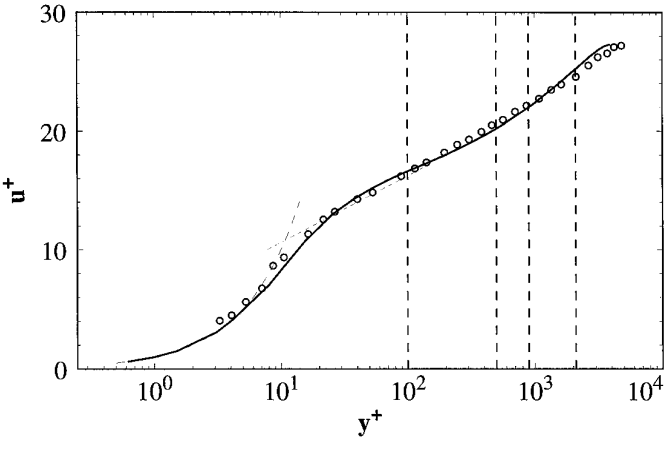

FIG. 17. Mean velocity profile of fully developed turbulent channel flow at Re_c = 109,410. ———, LES on 9-zone embedded grid; ○, Experiment Re_c = 120,000 [26]. Lines --- show the locations of the zonal boundaries.

Averaged subgrid scale shear stresses for multi-zone and single-zone large eddy simulations of turbulent channel flow at Reynolds number $\mathrm{Re}_m = 4.631 \times 10^4$ are shown in Fig. 18. As expected, the coarse grid calculations have a larger fraction of turbulent stresses in the subgrid-scale motions. Most significantly, the subgrid scale shear stresses in each zone follow the profiles of the single-zone simulations with the same resolution as in the corresponding zone. The same trend is observed in high Reynolds number LES. This correct behavior of the turbulent stresses is attributed to the robustness and consistency of the dynamic subgrid-scale model.

5. CONCLUSIONS

A B-spline based method on zonal embedded grids was developed and applied to computations of two test flows and DNS and LES of turbulent channel flow. The major advantage of this new method is that it allows a reduction in the computational costs of complex turbulent flow simulations by introducing zonal embedded grids.

The method was successfully tested in the problem of propagation of small disturbances in a channel flow and the problem of the vortex dipole rebound from the wall. In the latter test, it was shown that the zonal boundary did not affect either the structure or the strength of the vortices.

The DNS and LES calculations of a fully developed turbulent channel flow indicated that the results on the zonal embedded grid were in very good agreement with previously published numerical and experimental results obtained for the same flow. The zonal grid calculations needed only a fraction of the CPU time and memory re-

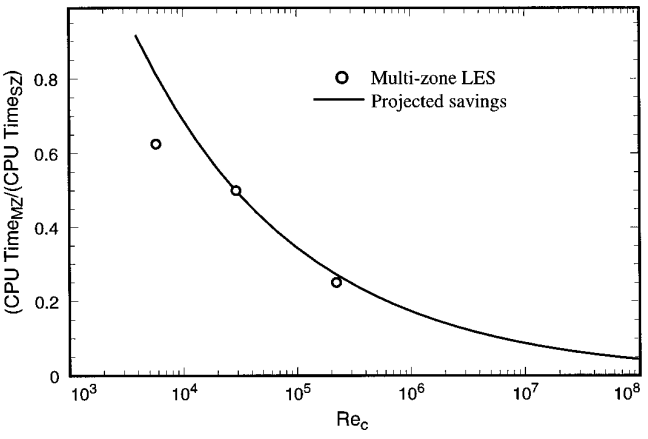

FIG. 19. Estimated CPU time savings as a function of Reynolds number. The solid curve is obtained using the estimate for nested grids suggested by Chapman [16]. The symbols are the estimated savings in our simulations.

quired for the single-zone grid calculation with the same near-wall grid density.

Figure 19 shows estimated savings in CPU time provided by using a zonal embedded grid in computations of turbulent boundary layers. It shows the ratio of the CPU time required for a multi-zone grid simulation to the CPU time required for a single-zone grid simulation as a function of the Reynolds number. It is clear that the most savings are realized in computing high Reynolds number flows.

ACKNOWLEDGMENTS

The financial support of this work by the Office of Naval Research under Grant No. N0014-94-1-0165 is gratefully acknowledged. The computer resources are provided by the computer facilities of NASA Ames Research Center.

REFERENCES

1. P. Moin and J. Jimenez, AIAA Paper, AIAA-93-3099, 1993 (unpublished).
2. J. W. Deardorff, *J. Fluid Mech.* **41,** 453 (1970).
3. U. Schumann, *J. Comput. Phys.* **18,** 376 (1975).
4. M. M. Rai and P. Moin, *J. Comput. Phys.* **109,** 169 (1993).
5. M. M. Rai, *Comput. Fluids* **14**(3), 295 (1986).
6. Y. Kallinderis, *J. Comput. Phys.* **98,** 129 (1992).
7. Y. Zang and R. L. Street, *Int. J. Numer. Methods Fluids* **20,** 341 (1995).
8. J. Y. Tu and L. Fuchs, *Int. J. Numer. Methods Fluids* **15,** 693 (1992).
9. C. Canuto, M. Y. Hussaini, A. Quarteroni, and T. A. Zang, *Spectral Methods in Fluid Dynamics* (Springer-Verlag, Berlin, 1988).
10. C. de Boor, *A Practical Guide to Splines* (Springer-Verlag, Berlin, 1978).
11. R. Moser, K. Shariff, P. Loulou, and A. G. Kravchenko, in preparation.
12. A. M. Davies, *J. Comput. Phys.* **27,** 123 (1978).
13. K. N. S. Kasi Viswanadham and S. R. Koneru, *Comput. Methods Appl. Mech. Engrg.* **108,** 201 (1993).
14. J. Kim, P. Moin, and R. Moser, *J. Fluid Mech.* **177,** 133 (1987).
15. P. R. Spalart, R. D. Moser, and M. M. Rogers, *J. Comput. Phys.* **96,** 297 (1991).
16. D. Chapman, *AIAA J.* **17**(12), 1293 (1979).
17. S. Orszag, *J. Comput. Phys.* **50,** 689 (1971).
18. M. R. Malik, T. A. Zang, and M. Y. Hussaini, *J. Comput. Phys.* **61,** 64 (1985).
19. P. Orlandi, *Phys. Fluids A* **2**(8), 1429 (1990).
20. M. Germano, U. Piomelli, P. Moin, and W. H. Cabot, *Phys. Fluids A* **3**(7), 1760 (1991).
21. U. Piomelli, *Phys. Fluids A* **5**(6), 1484 (1993).
22. D. K. Lilly, *Phys. Fluids A* **4**(3), 633 (1992).
23. A. K. M. F. Hussain and W. C. Reynolds, *Report No.* FM-*6*, Dept. of Mech. Eng., Stanford, 1970 (unpublished).
24. T. Wei and W. W. Willmarth, *J. Fluid Mech.* **204,** 57 (1989).
25. S. R. Smith and S. P. Metzler, *J. Fluid Mech.* **129,** 27 (1983).
26. G. Comte-Bellot, Ph.D. thesis, University of Grenoble, 1963 (unpublished).